International Journal of Minerals, Metallurgy and Materials
Volume 26, Number 3, March 2019, Page 319
https://doi.org/10.1007/s12613-019-1740-x

Anisotropy in mechanical properties and corrosion resistance of 316L stainless steel fabricated by selective laser melting

Xiao-qing Ni[1)], *De-cheng Kong*[2)], *Ying Wen*[2)], *Liang Zhang*[1)], *Wen-heng Wu*[1)], *Bei-bei He*[1)], *Lin Lu*[1)], *and De-xiang Zhu*[1)]

1) Shanghai Engineering Research Center of 3D Printing Materials, Shanghai Research Institute of Materials, Shanghai 200437, China
2) Corrosion and Protection Center, Key Laboratory for Corrosion and Protection (MOE), University of Science and Technology Beijing, Beijing 100083, China
(Received: 24 June 2018; revised: 29 July 2018; accepted: 25 September 2018)

Abstract: The corrosion behavior and mechanical properties of 316L stainless steel (SS) fabricated via selective laser melting (SLM) were clarified by potentiodynamic polarization measurements, immersion tests, and tensile experiments. The microstructural anisotropy of SLMed 316L SS was also investigated by electron back-scattered diffraction and transmission electron microscopy. The grain sizes of the SLMed 316L SS in the *XOZ* plane were smaller than those of the SLMed 316L SS in the *XOY* plane, and a greater number of low-angle boundaries were present in the *XOY* plane, resulting in lower elongation for the *XOY* plane than for the *XOZ* plane. The SLMed 316L was expected to exhibit higher strength but lower ductility than the wrought 316L, which was attributed to the high density of dislocations. The pitting potentials of the SLMed 316L samples were universally higher than those of the wrought sample in chloride solutions because of the annihilation of MnS or (Ca,Al)-oxides during the rapid solidification. However, the molten pool boundaries preferentially dissolved in aggressive solutions and the damage of the SLMed 316L in $FeCl_3$ solution was more serious after long-term service, indicating poor durability.

Keywords: selective laser melting; mechanical property; corrosion resistance; 316L stainless steel; anisotropy; molten pool boundary

1. Introduction

Three-dimensional (3D) printing is a burgeoning manufacturing technology that is attracting increasing attention. It is considered a potentially disruptive technology that will challenge traditional manufacturing methods across multiple industries [1–2]. 316L stainless steel (SS) has been widely used for components and structural materials in many industries because of its favorable durability, excellent welding performance, and good anti-corrosion characteristics [3–9]. However, the actual structure is complex and precise, thus making the traditional casting process time-consuming and expensive, especially when temporary replacement parts are required. In this case, selective laser melting (SLM), one of the 3D printing methods, offers substantial advantages in fabricating high-performance materials, such as more convenient molding and control of the composition and microstructure via powder mixing [10]. SLM manufacturing uses a high-power laser source to melt powders, followed by rapid solidification into solid parts. SLM has been the most popular metal powder bed fusion fabrication method among 3D printing techniques for metallic materials because of its greater productivity and economic advantages [11]. Thus far, the influence of printing parameters on the microstructure of selective laser melted (SLMed) parts, especially their porosity, cracks, and surface roughness, have been widely investigated [12–13]. The optimized process parameters usually result in enhanced mechanical properties [14–16]. However, the corrosion resistance and the durability of the SLMed parts have not drawn much attention [17–18], even though these properties play a critical role in determining the service life of the parts. It is not well known that corrosion causes an annual financial loss of US$4 trillion globally; half is due to corrosion damage and the other is attributed to corrosion protection [19–23]. Corrosion must be considered after the additive manufacturing technology has been widely

Corresponding author: Liang Zhang E-mail: lzhang0126@hotmail.com

applied for practical production [24–26].

Sander *et al*. [27] and Schaller *et al*. [28] found that SLMed 316L exhibits better pitting corrosion resistance in a NaCl solution, which was attributed to the refinement of oxide inclusions because MnS was rarely detected in their test materials. Meanwhile, the SLMed components on different sample planes tend to show different microstructural characteristics; thus, the mechanical and corrosion properties may differ [17,29], however, there are not many related studies about this.

In the present work, 316L SS was fabricated via SLM using optimized parameters (porosity < 0.3%), and the related microstructure was investigated by electron back-scattered diffraction (EBSD), transmission electron microscopy (TEM), and scanning electron microscopy (SEM). The mechanical properties of the sample were investigated via tensile experiments. The pitting corrosion resistance was evaluated via potentiodynamic polarization measurements in solutions with different chloride concentrations, and the durability of the specimens was compared by the ferric chloride immersion test. Meanwhile, the anisotropy in the SLMed 316L SS was also delineated. The results presented here provide a factual basis for the future application of SLMed 316L SS.

2. Experimental

2.1. Sample fabrication

The SLMed 316L samples were manufactured using gas-atomized 316L SS powder with a particle diameter from 15 to 45 μm and an average diameter of approximately 25 μm; these particles are smaller than those used in other studies [14,30]. The morphology of the gas-atomized powders is displayed in Fig. 1(a), and Fig. 1(b) shows the SLMed 316L products. The chemical compositions of the powders used for SLM were similar to the traditional wrought 316L, as listed in Table 1.

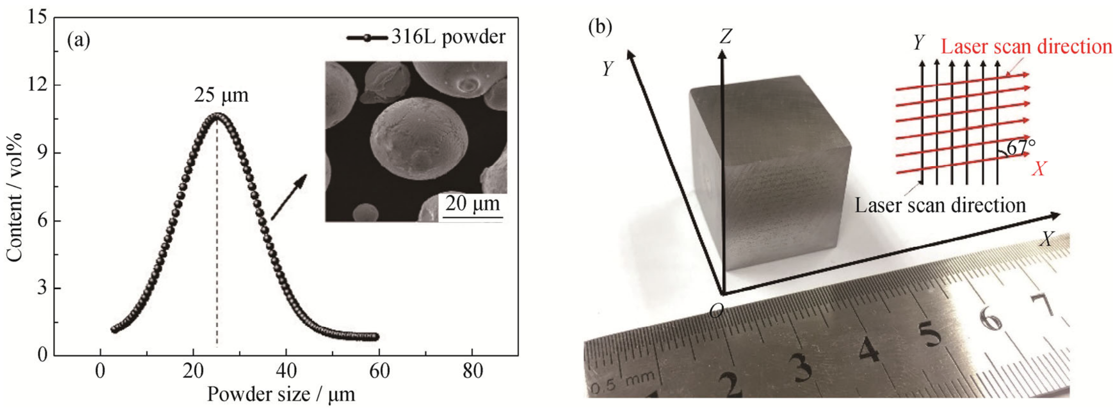

Fig. 1. Size distribution of the gas-atomized powder and the morphology of the powder particles (a) and the photograph of a SLMed sample along with a graphic showing the scanning direction (b).

Table 1. Chemical composition of the wrought 316L and the powder used in SLM processing wt%

Material	Ni	Cr	Mo	C	Mn	Si	P	S	N	Fe
Wrought	11.14	17.25	2.08	0.016	1.23	0.38	0.035	0.003	0.054	Bal.
Powder	11.08	17.36	2.02	0.013	1.19	0.36	0.032	0.002	0.052	Bal.

The method used to fabricate the sample is described in our previous work [16]. The density and microhardness of the fabricated sample were approximately 99.95% and HV 255, respectively. The *XOY* and *XOZ* surfaces were chosen as the working area for studying the anisotropy.

2.2. Microstructure characterization

The EBSD measurements were carried out at 20 kV with a scanning step of 1 μm. The samples were electropolished using 20vol% perchloric acid in liquid nitrogen for approximately 30 s prior to the measurements. To obtain the grain orientations and the grain-boundary densities, the EBSD data were analyzed using the TSL OIM Analysis 7 software. A transmission electron microscope was used to compare the microstructures of the wrought and SLMed 316L; the samples were prepared by double-injection electrolysis.

2.3. Tensile and electrochemical measurements

The tensile specimens were sequentially ground with increasingly fine emery paper to 2000 grit; the grinding direction was parallel to the loading direction. The samples were prepared according to the specifications in standard ASTM

E8: 2 mm thick, with a gauge length of 25 mm, and a gauge width of 6 mm.

Potentiodynamic polarization experiments were performed on a Princeton VersaStudio 3F electrochemical workstation with a conventional three-electrode cell in chloride solutions with different concentrations. The potentiodynamic polarization scans were all initiated at 250 mV less than the open-circuit potential and were conducted in the positive direction at a scanning rate of 0.1667 mV/s. The ferric chloride immersion experiments were carried out in a solution of 6wt% $FeCl_3$ and 0.05 M HCl. The tests were conducted using ferric chloride droplet on 316L for different periods, which was important for the following two reasons: 1) Crevice corrosion occurs easily at the side edge or the bottom during soaking. In this regard, Sander *et al.* [27] noted that the results of Trelewicz *et al.* [31], who reported that SLMed 316L exhibits reduced passivity in 0.1 M HCl, were possibly influenced by crevice corrosion. 2) Anisotropy was observed in the microstructural features of the SLMed matrix (e.g., grain size, composition, and molten pool boundaries (MPBs)), which precludes a simple comparison with the wrought 316L if the whole sample was soaked [17,32]. Thus, the ferric chloride droplet on the top surface of 316L was advantageous, and the samples were kept in a constant temperature and humidity chamber (40°C and 85% RH).

3. Results and discussion

3.1. Microstructure characterization

The microstructures of the traditional wrought 316L and SLMed 316L, including their grain sizes and the grain-boundary angles, were compared using inverse pole figures (Fig. 2). The 316L samples prepared by SLM were all austenite phase, and the wrought components exhibited larger and more regular polygonal grains than the SLMed samples. The surface on the *XOZ* plane presented more slender grains than that on the *XOY* plane, which was attributed to the greater temperature gradient in the *Z*-axis direction than in the *X*- and *Y*-directions during the laser melting process [33]. More twin boundaries were observed in wrought substrates with a 60° grain-boundary angle, whereas more low-angle boundaries were observed in the SLMed 316L. High-angle boundaries were more abundant in the *XOZ* plane than in the *XOY* plane for all of the SLMed samples because the heat conduction in the fabrication direction (*Z*-axis) is usually higher (a relatively faster cooling rate on the *XOZ* plane) than in the other two spatial directions (*X*- and *Y*-axes) because of the previously solidified material at the bottom.

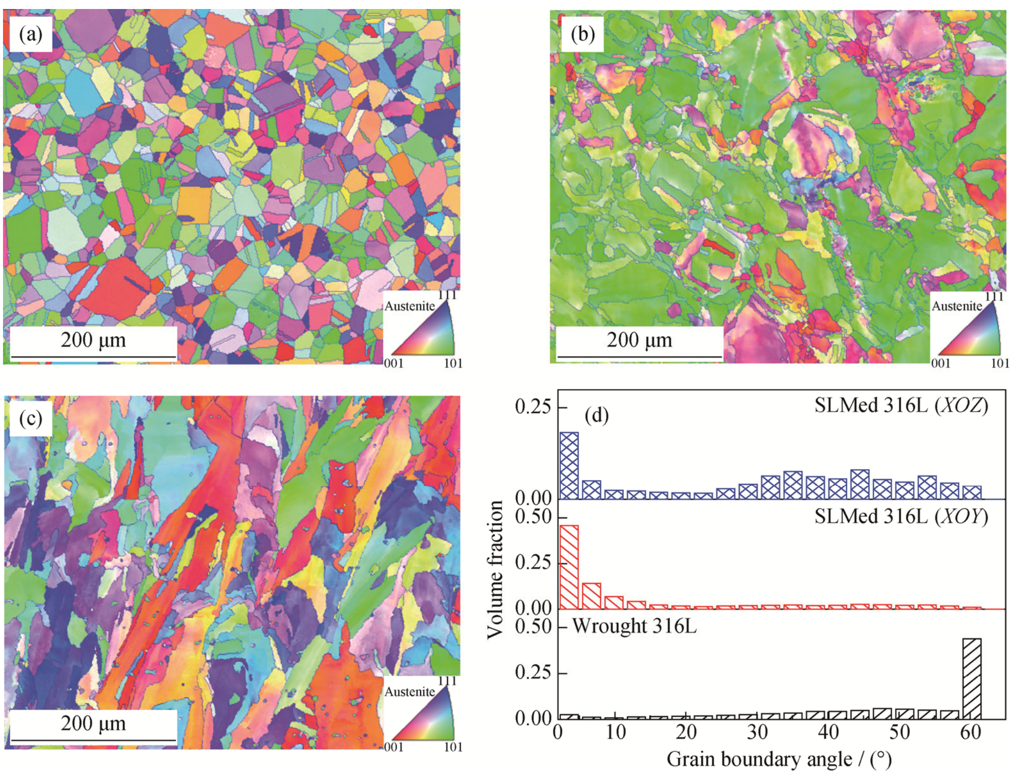

Fig. 2. Inverse pole figures of the 316L SS: (a) wrought; (b) SLMed (*XOY* plane); (c) SLMed (*XOZ* plane); (d) the corresponding grain-boundary angles.

3.2. Mechanical properties

The tensile curves of the wrought and SLMed 316L SS with different planes are displayed in Fig. 3, and the mechanical parameters are listed in Table 2. The values of the ultimate tensile strength (UTS) for the SLMed 316L (~620 MPa) were higher than those for the wrought 316L (~580 MPa), and the yield strength (YS) values of the SLMed 316L (560–570 MPa) were also greater than those of the wrought sample (290–300 MPa). However, the percentage elongation (e_f) after fracture for the SLMed 316L was smaller than that for the wrought 316L. Meanwhile, the e_f for the *XOY* plane (24.0%) was considerably smaller than that for the *XOZ* plane (38.0%), which is attributed to the greater number of low-angle boundaries in the *XOY* plane. By contrast, the grains grew along the *Z*-axis paralleling the stretch direction, as confirmed by the EBSD results.

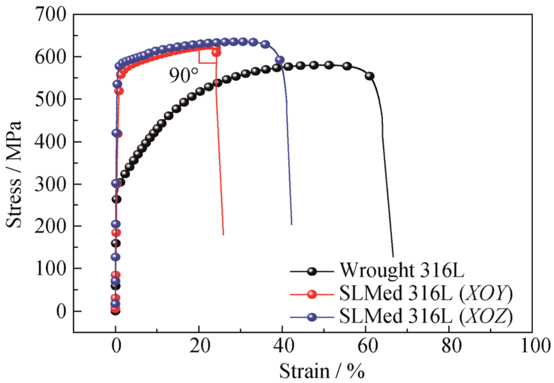

Fig. 3. Engineering stress vs. strain responses of the wrought and the SLMed 316L with different planes.

Table 2. Summary of the mechanical properties of 316L SS by SLM with different planes and the traditional wrought process

Material	YS / MPa	UTS / MPa	e_f / %
Wrought 316L	297.2 ± 5.2	581.6 ± 4.2	61.2 ± 4.8
SLMed 316L (*XOY*)	562.5 ± 6.7	616.6 ± 8.1	24.2 ± 3.0
SLMed 316L (*XOZ*)	572.2 ± 8.3	635.9 ± 6.2	38.6 ± 2.8

To elucidate the reason for the high UTS of the SLMed 316L, the morphologies of the wrought and SLMed 316L SS were observed by TEM, as shown in Fig. 4. Some dislocation lines were observed in the grains of the wrought 316L samples, whereas numerous subgrains were evident in the SLMed 316L; this phenomenon is in agreement with the results of other studies [15,34]. In addition, the subgrain boundaries of the SLMed samples were full of dislocation lines [35] and this high density of dislocations is attributable to the enrichment of misplaced molybdenum in the austenite lattice during high-speed solidification [15], which resulted in a high strength, as displayed in Fig. 3.

The fractographic morphologies of the 316L after tensile experiments are displayed in Fig. 5. Typical dimples were observed in the metallic fracture for the wrought 316L, whereas pores existed in the SLMed 316L samples. The premature instability and fracture of the *XOY* plane for the SLMed 316L are attributed to the large number of voids, as displayed in Fig. 5(b). Meanwhile, the aspect ratio was larger for the pores on the *XOY* plane than for those on the *XOZ* plane, which also accelerates fracture [36].

3.3. Corrosion behavior

Fig. 6 shows the potentiodynamic polarization curves for the wrought and SLMed 316L in chloride solutions with different concentrations. The corrosion potentials of the wrought and SLMed 316L did not substantially change in NaCl solutions (approximately −0.21 V vs. SCE), and the SLMed 316L samples all exhibited a higher pitting potential than the wrought samples in chloride-containing solutions. These observations are consistent with previous reports that the SLM process might reduce the size and content of inclusions, such as MnS or (Ca,Al)-oxides [27,37–38].

Generally, the pitting potentials decreased linearly with lg[Cl^-], as proposed on the basis of the point defect model [39–43]. Fig. 6(c) shows that the absolute slope for the wrought samples was greater than that for the SLMed samples, indicating that the wrought 316L was more

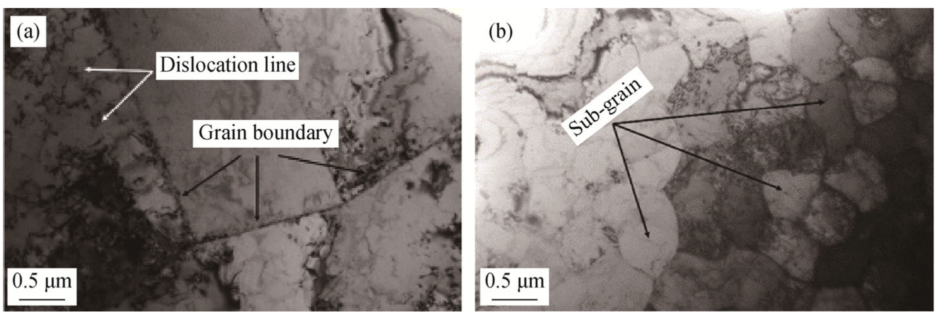

Fig. 4. Transmission electron microscopy results (bright field): (a) wrought 316L; (b) SLMed 316L.

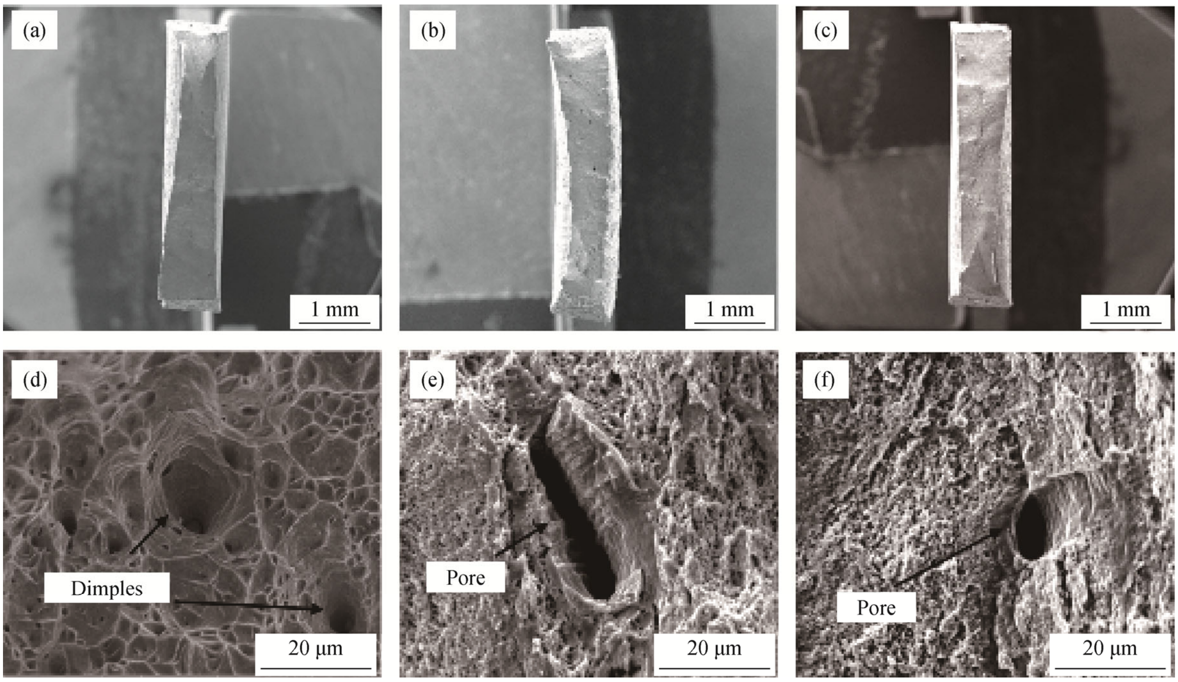

Fig. 5. SEM microscopic morphologies of the fractographic 316L: (a) and (d) wrought 316L; (b) and (e) SLMed 316L (*XOY*); (c) and (f) SLMed 316L (*XOZ*).

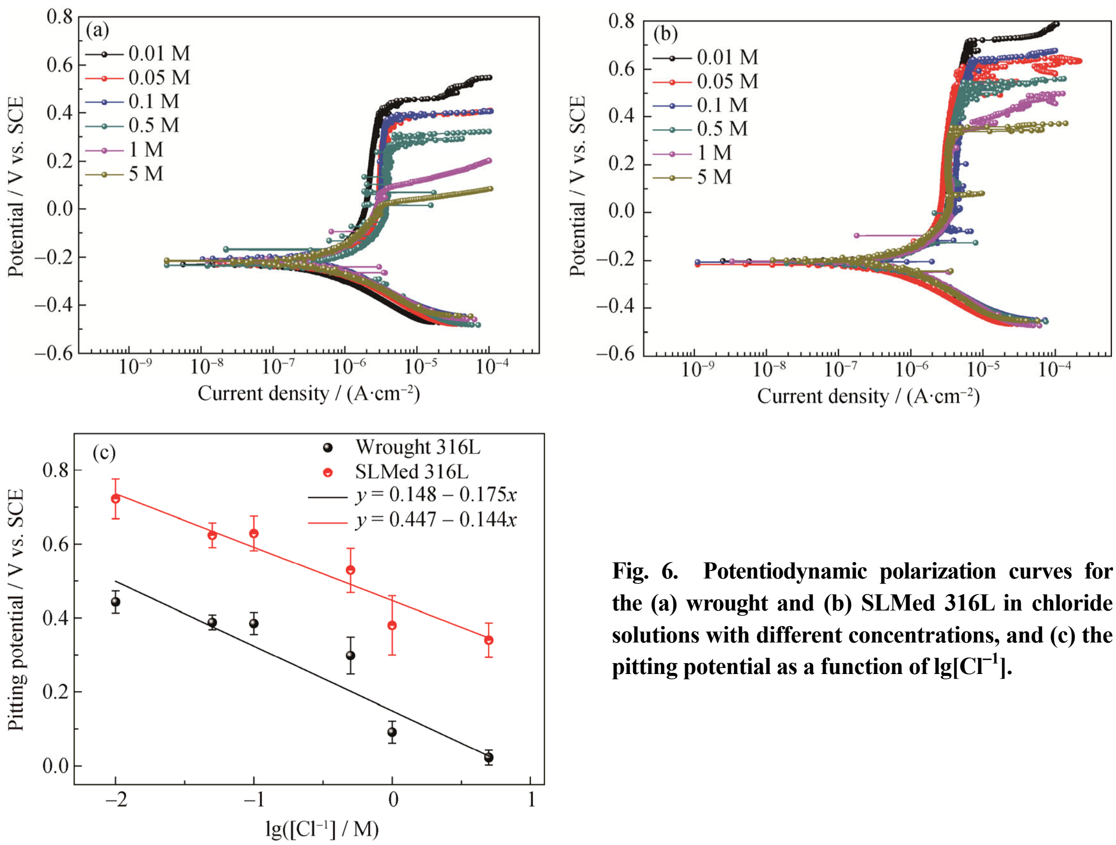

Fig. 6. Potentiodynamic polarization curves for the (a) wrought and (b) SLMed 316L in chloride solutions with different concentrations, and (c) the pitting potential as a function of lg[Cl^{-1}].

sensitive to the chloride activity. To confirm the cause of the pitting corrosion, the EDS mapping images of the pits on the wrought 316L are shown in Figs. 7(a)–7(i), and the results confirm that the pits were induced by the formation of

(Al,Ca)-oxide inclusions [37–38].

Fig. 7(j) displays a typical pit on the SLMed 316L; no inclusions were observed. In our SLMed 316L substrate, MnS or (Al,Ca)-oxide inclusions were also not found because of the rapid solidification rates (typically ~10^7 K/s), where 0.1–10 s was available for the nucleation and diffusional growth of the inclusions in the wrought sample [37,44]. Thus, the modification of inclusions in the SLMed 316L improved the pitting corrosion resistance [27]. In the SLMed 316L, numerous subgrains and nanoscale precipitations (~180 nm in Fig. 7(k)) were observed; the nanoscale precipitations were attributed to the accumulation of O, Al, Si, and Mn, as displayed in Fig. 7(l) [15,45]. The precipitations of this scale did not adversely affect the corrosion resistance [28,46].

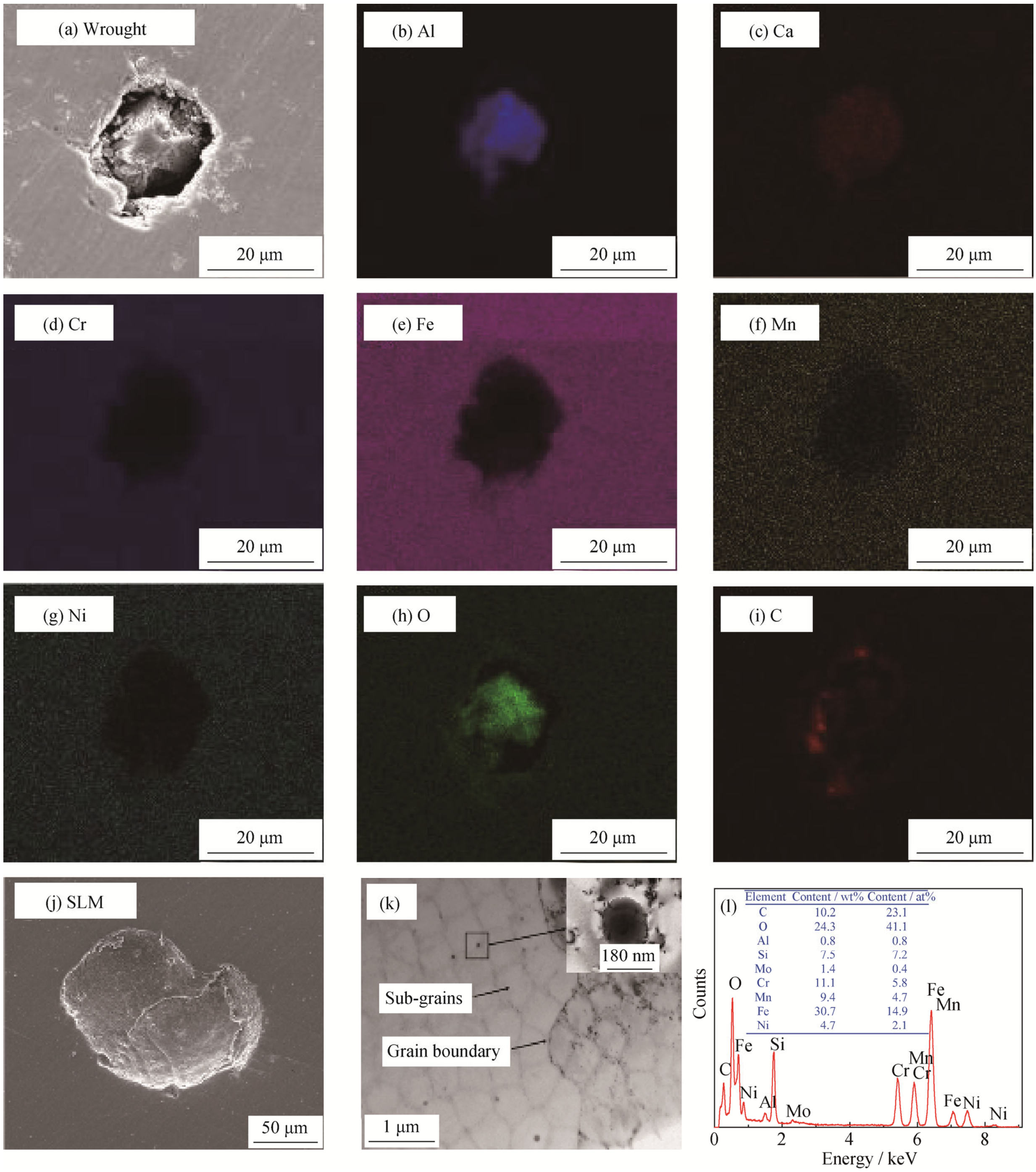

Element	Content / wt%	Content / at%
C	10.2	23.1
O	24.3	41.1
Al	0.8	0.8
Si	7.5	7.2
Mo	1.4	0.4
Cr	11.1	5.8
Mn	9.4	4.7
Fe	30.7	14.9
Ni	4.7	2.1

Fig. 7. EDS analysis results for typical pitting on the wrought 316L (a–i) and typical pitting morphology of the SLMed 316L (j), and TEM results for the SLMed 316L substrate (k) and the related EDS results of the precipitations (l).

Fig. 8 shows the surface morphologies of the wrought and SLMed 316L immersed in ferric chloride solution for 12 h. Numerous small pits were observed on the wrought 316L, as displayed in Fig. 8(c), whereas unwounded areas were observed on the SLMed 316L except for the MPBs displayed in Fig. 8(f). We propose that the corrosion attack occurred preferentially at the MPBs in the SLMed 316L, whereas the other locations in the sample exhibited better corrosion resistance. These results do not conflict with those corresponding to the samples immersed in ferric chloride solutions because those surface defects (MPBs or pores) can trigger corrosion in such aggressive environments. Geenen *et al*. [47] also confirmed that the pores in the SLMed matrix were preferential corrosion sites, and Schaller *et al*. [36] further concluded that the reduced corrosion resistance of the SLMed SS corresponds to the pores with diameters ≥ 50 μm. For a single pore, the active spot also increased slightly in activity with increased exposure time when monitored by SEM and thus led to poor durability of the SLMed parts [28].

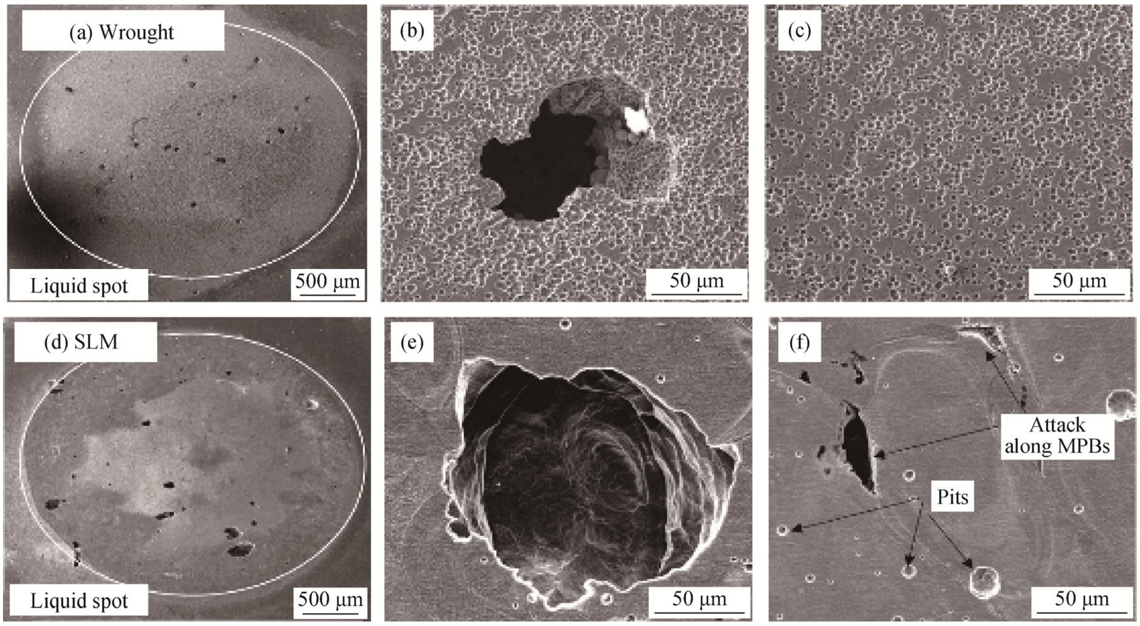

Fig. 8. Surface morphologies of the wrought (a–c) and SLMed (d–f) 316L immersed in iron(III) chloride solution for 12 h.

At the initial stage (1 min in Figs. 9(a) and 9(e)), numerous small pits were evident on the wrought 316L but not on the SLMed 316L, except for the highlighted MPBs. With increasing exposure time, the corrosion attack on the SLMed 316L initiated at the MPBs and developed rapidly. The pits of the SLMed parts after a long-term immersion were much deeper than those of the wrought substrates, as displayed in Fig. 9(i). Meanwhile, the subsurface defects could also merge with pits and grow into the metal. As in this case, further heat treatments need to be considered to homogenize the aforementioned nonequilibrium structures before SLM can be applied on a large scale.

4. Conclusions

The microstructures of 316L SS fabricated by SLM were investigated by EBSD, TEM, and SEM, and its anticorrosion performance and mechanical properties were evaluated via potentiodynamic polarization experiments, immersion tests, and tensile experiments. The main conclusions were drawn as follows:

(1) The *XOZ* plane for the SLMed 316L exhibited more slender grains than the *XOY* plane (equiaxed grains), and wrought substrates with a 60° grain boundary angle contained more twin boundaries; by contrast, more low-angle boundaries were present in the SLMed 316L.

(2) More low-angle boundaries were observed in the *XOY* plane than in the *XOZ* plane for the SLMed 316L, resulting in a low elongation as well as a large aspect ratio for the pores on the *XOY* plane.

(3) The pitting potentials of the SLMed 316L were universally higher than those of the wrought in chloride solutions with different concentrations because of the annihilation of MnS or (Ca,Al)-oxides during the rapid solidification. The MPBs dissolved faster in ferric chloride solution, and the pit depth of the SLMed 316L increased faster than the wrought, indicating poor durability for the SLMed parts in aggressive environments.

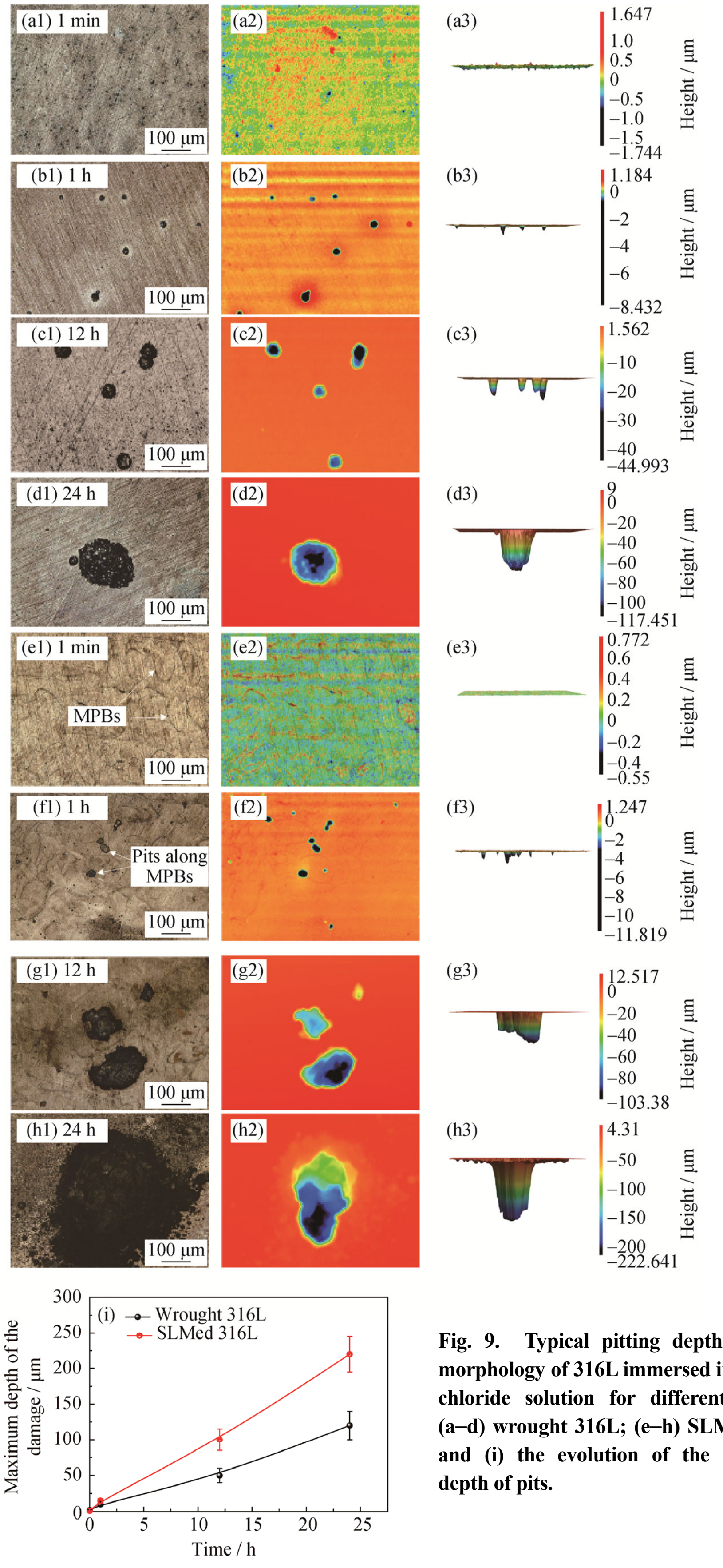

Fig. 9. Typical pitting depth and 3-D morphology of 316L immersed in iron(III) chloride solution for different periods: (a–d) wrought 316L; (e–h) SLMed 316L; and (i) the evolution of the maximum depth of pits.

Acknowledgements

This work was financially supported by the Shanghai Materials Genome Institute No. 5 (No. 16DZ2260605), the Shanghai Sailing Program (No. 17YF1405400), and the Project to Strengthen Industrial Development at the Grass-roots Level (No. TC160A310/19).

References

[1] T. DebRoy, H.L. Wei, J.S. Zuback, T. Mukherjee, J.W. Elmer, J.O. Milewski, A.M. Beese, A. Wilson-Heid, A. De, and W. Zhang, Additive manufacturing of metallic components–process, structure and properties, *Prog. Mater. Sci.*, 92(2018), p. 112.

[2] H.P. Duan, X. Liu, X.Z. Ran, J. Li, and D. Liu, Mechanical properties and microstructure of 3D-printed high Co–Ni secondary hardening steel fabricated by laser melting deposition, *Int. J. Miner. Metall. Mater.*, 24(2017), p. 1027.

[3] F. Mao, C. Dong, and D.D. Macdonald, Effect of octadecylamine on the corrosion behavior of type 316SS in acetate buffer, *Corros. Sci.*, 98(2015), p. 192.

[4] X.W. Lei, H.Y. Wang, F.X. Mao, J.P. Zhang, A.Q. Fu, Y.R. Feng, and D.D. Macdonald, Electrochemical behaviour of martensitic stainless steel after immersion in a H_2S-saturated solution, *Corros. Sci.*, 131(2018), p. 164.

[5] C.F. Dong, A.Q. Fu, X.G. Li, and Y.F. Cheng, Localized EIS characterization of corrosion of steel at coating defect under cathodic protection, *Electrochim. Acta*, 54(2008), No. 2, p. 628.

[6] Y.B. Hu, C.F. Dong, M. Sun, K. Xiao, P. Zhong, and X.G. Li, Effects of solution ph and Cl^- on electrochemical behaviour of an aermet100 ultra-high strength steel in acidic environments, *Corros. Sci.*, 53(2011), No. 12, p. 4159.

[7] S.J. Gao, C.F. Dong, H. Luo, K. Xiao, X.M. Pan, and X.G. Li, Scanning electrochemical microscopy study on the electrochemical behavior of CrN film formed on 304 stainless steel by magnetron sputtering, *Electrochim. Acta*, 114(2013), p. 233.

[8] L. Fan, H.Y. Chen, Y.H. Dong, L.H. Dong, and Y.S. Yin, Wear and corrosion resistance of laser-cladded Fe-based composite coatings on AISI 4130 steel, *Int. J. Miner. Metall. Mater.*, 25(2018), No. 6, p. 716.

[9] Y.Z. Zhang, C. Huang, and R. Vilar, Microstructure and properties of laser direct deposited $CuNi_{17}Al_3Fe_{1.5}Cr$ alloy, *Int. J. Miner. Metall. Mater.*, 18(2011), No. 3, p. 325.

[10] Y. Kok, X.P. Tan, P. Wang, M.L.S. Nai, N.H. Loh, E. Liu, and S.B. Tor, Anisotropy and heterogeneity of microstructure and mechanical properties in metal additive manufacturing: A critical review, *Mater. Des.*, 139(2018), p. 565.

[11] S. Van Bael, Y.C. Chai, S. Truscello, M. Moesen, G. Kerckhofs, H. Van Oosterwyck, J.P. Kruth, and J. Schrooten, The effect of pore geometry on the in vitro biological behavior of human periosteum-derived cells seeded on selective laser-melted Ti6Al4V bone scaffolds, *Acta Biomater.*, 8(2012), No. 7, p. 2824.

[12] G. Miranda, S. Faria, F. Bartolomeu, E. Pinto, S. Madeira, A. Mateus, P. Carreira, N. Alves, F.S. Silva, and O. Carvalho, Predictive models for physical and mechanical properties of 316L stainless steel produced by selective laser melting, *Mater. Sci. Eng. A*, 657(2016), p. 43.

[13] F.X. Xie, X.B. He, S.L. Cao, and X.H. Qu, Structural and mechanical characteristics of porous 316L stainless steel fabricated by indirect selective laser sintering, *J. Mater. Process. Technol.*, 213(2013), No. 6, p. 838.

[14] A. Röttger, K. Geenen, M. Windmann, F. Binner, and W. Theisen, Comparison of microstructure and mechanical properties of 316L austenitic steel processed by selective laser melting with hot-isostatic pressed and cast material, *Mater. Sci. Eng. A*, 678(2016), p. 365.

[15] K. Saeidi, X. Gao, Y. Zhong, and Z.J. Shen, Hardened austenite steel with columnar sub-grain structure formed by laser melting, *Mater. Sci. Eng. A*, 625(2015), p. 221.

[16] X.Q. Ni, D.C. Kong, W.H. Wu, L. Zhang, C.F. Dong, B.B. He, L. Lu, K.Q. Wu, and D.X. Zhu, Corrosion behavior of 316L stainless steel fabricated by selective laser melting under different scanning speeds, *J. Mater. Eng. Perform.*, 27(2018), No. 7, p. 3667.

[17] N.W. Dai, L.C. Zhang, J.X. Zhang, X. Zhang, Q.Z. Ni, Y. Chen, M.L. Wu, and C. Yang, Distinction in corrosion resistance of selective laser melted Ti–6Al–4V alloy on different planes, *Corros. Sci.*, 111(2016), p. 703.

[18] G.Q. Yang, J.K. Mo, Z.Y. Kang, F.A. List, J.B. Green, S.S. Babu, and F.Y. Zhang, Additive manufactured bipolar plate for high-efficiency hydrogen production in proton exchange membrane electrolyzer cells, *Int. J. Hydrogen Energy*, 42(2017), No. 21, p. 14734.

[19] B.R. Hou, X.G. Li, X.M. Ma, C.W. Du, D.W. Zhang, M. Zheng, W.C. Xu, D.Z. Lu, and F.B. Ma, The cost of corrosion in China, *npj Mater. Degrad.*, 1(2017), art. No. 4.

[20] X.G. Li, D.W. Zhang, Z.Y. Liu, Z. Li, C.W. Du, and C.F. Dong, Materials science: Share corrosion data, *Nature*, 527(2015), No. 7579, p. 441.

[21] D.C. Kong, C.F. Dong, Y.H. Fang, K. Xiao, C.Y. Guo, G. He, and X.G. Li, Long-term corrosion of copper in hot and dry atmosphere in Turpan, China, *J. Mater. Eng. Perform.*, 25(2016), No. 7, p. 2977.

[22] D.C. Kong, C.F. Dong, X.Q. Ni, A.N. Xu, C. He, K. Xiao, and X.G. Li, Long-term polarisation and immersion for copper corrosion in high-level nuclear waste environment, *Mater. Corros.*, 68(2017), No. 10, p. 1070.

[23] D.C. Kong, C.F. Dong, X.Q. Ni, C. Man, K. Xiao, and X.G. Li, Insight into the mechanism of alloying elements (Sn,Be) effect on copper corrosion during long-term degradation in harsh marine environment, *Appl. Surf. Sci.*, 455(2018), p. 543.

[24] H. Luo, C.F. Dong, K. Xiao, and X.G. Li, Characterization of passive film on 2205 duplex stainless steel in sodium thiosulphate solution, *Appl. Surf. Sci.*, 258(2011), No. 1, p. 631.

[25] C.F. Dong, Z.Y. Liu, X.G. Li, and Y.F. Cheng, Effects of hydrogen-charging on the susceptibility of X100 pipeline steel to hydrogen-induced cracking, *Int. J. Hydrogen Energy*, 34(2009), No. 24, p. 9879.

[26] C.F. Dong, X.G. Li, Z.Y. Liu, and Y.R. Zhang, Hydrogen-induced cracking and healing behaviour of X70 steel, *J. Alloys Compd.*, 484(2009), No. 1-2, p. 966.

[27] G. Sander, S. Thomas, V. Cruz, M. Jurg, N. Birbilis, X. Gao, M. Brameld, and C.R. Hutchinson, On the corrosion and metastable pitting characteristics of 316L stainless steel produced by selective laser melting, *J. Electrochem. Soc.*, 164(2017), No. 6, p. 250.

[28] R.F. Schaller, A. Mishra, J.M. Rodelas, J.M. Taylor, and E.J. Schindelholz, The role of microstructure and surface finish on the corrosion of selective laser melted 304L, *J. Electrochem. Soc.*, 165(2018), No. 5, p. 234.

[29] W.E. Frazier, Metal additive manufacturing: A review, *J. Mater. Eng. Perform.*, 23(2014), No. 6, p. 1917.

[30] P. Guo, B. Zou, C.Z. Huang, and H.B. Gao, Study on microstructure, mechanical properties and machinability of efficiently additive manufactured AISI 316L stainless steel by high-power direct laser deposition, *J. Mater. Process. Technol.*, 240(2017), p. 12.

[31] J.R. Trelewicz, G.P. Halada, O.K. Donaldson, and G. Manogharan, Microstructure and corrosion resistance of laser additively manufactured 316L stainless steel, *JOM*, 68(2016), No. 3, p. 850.

[32] Y. Chen, J.X. Zhang, X.H. Gu, N.W. Dai, P. Qin, and L.C. Zhang, Distinction of corrosion resistance of selective laser melted Al–12Si alloy on different planes, *J. Alloys Compd.*, 747(2018), p. 648.

[33] V.A. Popovich, E.V. Borisov, A.A. Popovich, V.S. Sufiiarov, D.V. Masaylo, and L. Alzina, Functionally graded inconel 718 processed by additive manufacturing: Crystallographic texture, anisotropy of microstructure and mechanical properties, *Mater. Des.*, 114(2017), p. 441.

[34] D.C. Kong, X.Q. Ni, C.F. Dong, X.W. Lei, L. Zhang, C. Man, J.Z. Yao, X.Q. Cheng, and X.G. Li, Bio-functional and anti-corrosive 3D printing 316L stainless steel fabricated by selective laser melting, *Mater. Des.*, 152(2018), p. 88.

[35] D.C. Kong, X.Q. Ni, C.F. Dong, L. Zhang, C. Man, J.Z. Yao, K. Xiao, and X.G. Li, Heat treatment effect on the microstructure and corrosion behavior of 316L stainless steel fabricated by selective laser melting for proton exchange membrane fuel cells, *Electrochim. Acta*, 276(2018), p. 293.

[36] R.F. Schaller, J.M. Taylor, J. Rodelas, and E.J. Schindelholz, Corrosion properties of powder bed fusion additively manufactured 17-4 PH stainless steel, *Corrosion*, 73(2017), No. 7, p. 796.

[37] S.Q. Zheng, C.Y. Li, Y.M. Qi, L.Q. Chen, and C.F. Chen, Mechanism of (Mg,Al,Ca)-oxide inclusion-induced pitting corrosion in 316L stainless steel exposed to sulphur environments containing chloride ion, *Corros. Sci.*, 67(2013), p. 20.

[38] C. Man, C.F. Dong, K. Xiao, Q. Yu, and X.G. Li, The combined effect of chemical and structural factors on pitting corrosion induced by MnS–(Cr,Mn,Al)O duplex inclusions, *Corrosion*, 74(2018), No. 3, p. 312.

[39] D.D. Macdonald, The history of the point defect model for the passive state: A brief review of film growth aspects, *Electrochim. Acta*, 56(2011), No. 4, p. 1761.

[40] D.C. Kong, C.F. Dong, Z.R. Zheng, F.X. Mao, A.N. Xu, X.Q. Ni, C. Man, J.Z. Yao, K. Xiao, and X.G. Li, Surface monitoring for pitting evolution into uniform corrosion on Cu–Ni–Zn ternary alloy in alkaline chloride solution: *ex-situ* LCM and *in-situ* SECM, *Appl. Surf. Sci.*, 440(2018), p. 245.

[41] D.C. Kong, A.N. Xu, C.F. Dong, F.X. Mao, K. Xiao, X.G. Li, and D.D. Macdonald, Electrochemical investigation and ab initio computation of passive film properties on copper in anaerobic sulphide solutions, *Corros. Sci.*, 116(2017), p. 34.

[42] D.C. Kong, C.F. Dong, M.F. Zhao, X.Q. Ni, C. Man, and X.G. Li, Effect of chloride concentration on passive film properties on copper, *Corros. Eng. Sci. Technol.*, 53(2017), No. 2, p. 122.

[43] C.F. Dong, F.X. Mao, S.J. Gao, S. Sharifi-Asl, P. Lu, and D.D. Macdonald, Passivity breakdown on copper: Influence of temperature, *J. Electrochem. Soc.*, 163(2016), No. 13, p. 707.

[44] M. Suzuki, R. Yamaguchi, K. Murakami, and M. Nakada, Inclusion particle growth during solidification of stainless steel, *ISIJ Int.*, 41(2007), No. 3, p. 247.

[45] Q. Chao, V. Cruz, S. Thomas, N. Birbilis, P. Collins, A. Taylor, P.D. Hodgson, and D. Fabijanic, On the enhanced corrosion resistance of a selective laser melted austenitic stainless steel, *Scripta Mater.*, 141(2017), p. 94.

[46] W.D. Stewart and D.E. Williams, The initiation of pitting corrosion on austenitic stainless steel: On the role and importance of sulfide inclusions, *Corros. Sci.*, 33(1992), No. 3, p. 457.

[47] K. Geenen, A. Röttger, and W. Theisen, Corrosion behavior of 316L austenitic steel processed by selective laser melting, hot-isostatic pressing, and casting, *Mater. Corros.*, 68(2017), No. 7, p. 764.